



3-D CdS@NiCo layered double hydroxide core-shell photoelectrocatalyst used for efficient overall water splitting

Azam Pirkarami^a, Sousan Rasouli^{a,*}, Ebrahim Ghasemi^{b,c,*}

^a Department of Nanomaterials & Nanocoatings, Institute for Color Science and Technology (ICST), Tehran, Iran

^b Inorganic Pigment and Glazes Department, Institute for Color Science and Technology, Tehran, Iran

^c Center of Excellence for Color Science and Technologies, Institute for Color Science and Technology, Tehran, Iran

ARTICLE INFO

Keywords:

CdS@NiCo-LDH/NF

Water splitting

Oxygen evolution

Layered double hydroxide (LDH)

Hydrogen evolution

ABSTRACT

Designing durable and highly active photoelectrocatalysts for overall water splitting is very challenging. Here, we report an easy method for synthesizing a highly efficient three-dimensional core-shell photoelectrocatalyst. This catalyst consists of cadmium sulfide as the core and nickel-cobalt layered double hydroxide as the shell, thus CdS@NiCo-LDH. The advantages of this catalyst are high specific surface area, rapid transfer of electrons, and open channels for the release of gaseous products, which lead to better oxygen evolution reaction (OER) and hydrogen evolution reaction (HER) in alkaline environments. The use of this catalyst in water decomposition for OER allows current density values of 10, 100, 500, and 1000 mA cm⁻² at a voltage of 132, 198, 306, and 309 mV, respectively. Also, using this catalyst for HER allows current density values of 10 and 100 mA cm⁻² at a voltage of 379 and 202 mV respectively.

1. Introduction

The increased use of fossil fuels generates excessive carbon dioxide, and this necessitates finding clean alternative resources [1]. Water splitting through the photoelectrochemical (PEC) process has attracted much attention due to increased demand for renewable energy. In most PEC devices, photocathodes and photoanodes are used for the generation of hydrogen and oxygen, respectively. These methods can contribute to the resolution of the environmental and economic problems emanating from fossil fuels [2].

Hydrogen is a source of clean, efficient, and renewable energy [3,4]. An environmentally-friendly and economical way of producing hydrogen, which can ideally replace fossil fuels, is the photoelectrochemical splitting of water in the two half-reactions of hydrogen evolution reaction (HER) and oxygen evolution reaction (OER) [5]. Currently, much research attempt is aimed at building strong catalysts for overall water splitting. A good catalyst should be inexpensive and at the same time stable and resistant for HER [6]. The latter two characteristics can be found in catalysts such as iridium dioxide (IrO₂), ruthenium dioxide (RuO₂), and platinum. However, these catalysts are expensive because they are rare in nature [7–9]. Over the years, significant advances have been made in the production of high-performance catalysts which are based on carbon, transition metals, and layered double hydroxides (LDH) [10]. Most OER catalysts can perform

well in alkaline environments, but the same cannot be said about HER catalysts. Therefore, it is very important to develop an HER catalyst that is not only good for alkaline environments, but can also be satisfactorily efficient in overall water splitting.

Much attention has been paid to two-dimensional (2-D) layered materials due to their new structural features in catalysis and energy storage [11]. A viable 2-D layered material is LDH as it is cheap and plentiful and can be conveniently scaled up [12,13]. LDH-based materials can make efficient OER catalysts because of their unique layered structure, which allows water molecules to diffuse and gaseous products to release quickly. For example, Luo et al. [14] simultaneously used two perovskite solar cells, each having a high open-circuit voltage of over 1.06 V, which is enough for overall water splitting. Additionally, they employed a bi-functional NiCo-LDH electrocatalyst to substantially reduce the over-potentials of OER and HER. Other LDH-based catalysts reported in the literature for water splitting include TiO₂ core-NiCr LDH shell [15] and TiO₂/ZnFe-LDH [16]. However, their performance still needs to be improved, and the voltage required to generate high current density (100 mA cm⁻²) does not meet the practical applications [17].

Study [18] used hierarchical nanowire arrays based on the ZnO core and the NiCo-LDH shell. These exhibited impressive performance in photoelectrochemical water decomposition with high stability and photocurrent density, which the authors ascribed to the excellent electrocatalytic activity of the CoNi-LDH shell and the core-shell

* Corresponding author.

E-mail addresses: sousan.rasouli96@gmail.com (S. Rasouli), eghasemi@icrc.ac.ir (E. Ghasemi).

<https://doi.org/10.1016/j.apcatb.2018.09.021>

Received 6 June 2018; Received in revised form 23 August 2018; Accepted 8 September 2018

Available online 09 September 2018

0926-3373/ © 2018 Published by Elsevier B.V.

integration, which in turn led to photo-generated electron-hole separation [19]. The design and construction of an electrode is an efficient method for increasing and maintaining catalytic activity. In particular, much attention has been paid to the nanostructure shell grown on conductive substrates such as the Ni foam, copper, and graphene due to the effective transfer of electrons, easy access to electrolytes, and a high specific surface area [20]. Shao et al. introduced a core-shell catalyst (ZnO@NiCo-LDH) grown on the fluorine-doped tin oxide (FTO) for efficient photocatalysis [21].

Chen et al. constructed the Cu₂O@NiFe core-shell grown on copper foam as an effective three-dimensional (3-D) electrocatalyst for OER [22]. The authors used copper core as a highly-conductive layer to compensate for the insufficient electrical conductivity of NiCo and to achieve dependable electron transition and better catalytic reactions.

In the present study, we introduce a novel photoelectrocatalyst (CdS@NiCo-LDH), consisting of cadmium sulfide (CdS) nanowire as the core and nickel-cobalt layered double hydroxide (NiCo-LDH) as the shell. Numerous studies have been reported on CdS nanoparticles due to their excellent photocatalytic properties and a good visible-light response [23,24]. CdS nanowires are employed because CdS has the ability to absorb visible light at short wavelengths of less than 516 nm, has a high conductivity, is inexpensive, and can be synthesized without difficulty [25]. We believe that the 3-D structure of the NiCo LDH nanoshell on the CdS core (CdS@NiCo-LDH) supported on the Ni foam can be a very attractive method for overall water splitting. This 3-D core-shell catalyst has a better mechanical integrity because CdS nanowires are grown exactly on the nickel foam and diffuse in the NiCo layers of LDH, thereby permitting favorable electron transfer. In addition, NiCo-LDH nanostructures are grown vertically on CdS nanowires, increasing the surface area of the catalyst and generating more active sites on the photoelectrocatalyst. Moreover, the high conductivity of the Ni foam and the NiCo-LDH shell effectively transfers electrons from the CdS core to the nanoshell and rapidly releases gaseous products. As a result, the 3-D core-shell catalyst can provide excellent HER and OER performance in an alkaline environment for efficient and effective overall water splitting.

This study is innovative in that the CdS@NiCo-LDH electrode is prepared through electrodeposition and hydrothermal synthesis. Moreover, we used LDH nanomaterials as we wanted water molecules to penetrate into the boundary between ions and the catalyst. This would improve the transfer of ions from the catalyst to the electrolyte and would reduce electrical resistance. Additionally, this catalyst presents a low over-potential, small Tafel slope, and great stability. Furthermore, 3-D CdS@NiCo-LDH core-shell nanoparticles uniformly grow on the surface of Ni foam, which leads to an increase in the number of active sites and ultimately raises performance levels and enhances adaptability [26]. Lastly, we believe the dual method used here for catalyst preparation can be employed to develop other catalysts based on transition metals.

2. Experimental section

2.1. Chemicals and reagents

A nickel foam with a thickness of 1.5 mm, a bulk porosity of 90–98 percent, and a bulk density of 0.15 to 0.45 g/cm³ with 5 to 120 cavities per inch was purchased from Latech Scientific Supply (Singapore). The other materials, all procured from Merck, were cobalt(II) nitrate hexahydrate (Co(NO₃)₂·6H₂O; ≥99%), cadmium acetate dihydrate (Cd(CH₃COO)₂·2H₂O; purity ≥99%), thiourea (NH₂CSNH₂), hexamethylenetetramine (C₆H₁₂N₄; ≥99%) hydrochloric acid (HCl; ≥99%), nickel (II) nitrate hexahydrate (Ni(H₂O)₆(NO₃)₂; ≥99%), ethanol (C₂H₆O; ≥99%), and potassium hydroxide (KOH). All the reactants were of the highest purity and were used without further purification. Deionized water was employed for chemical synthesis in a reaction autoclave (material: stainless steel shell and Teflon liner, volume: 130 mL, max.

temperature: 250 °C).

2.2. Fabrication of CdS@NiCo-LDH on the Ni foam

CdS was synthesized via a chemical oxidation method as follows. Initially, the Ni foam (3 × 5 cm) was placed for 8 min in an ultrasonic bath, containing hydrochloric acid (37%), deionized water and, ethanol. Then, the cleaned Ni foam was placed for 20 min in 70 mL of an aqueous solution that contained 1.9 M sodium hydroxide and 0.131 M ammonium sulfate. This changed the color of the Ni foam, which was subsequently washed with deionized water. Afterward, the Ni foam was placed in an oven at 170 °C for 30 min in order to obtain suitable conditions for the nucleation and calcination of the CdS nanoparticles. Cadmium acetate dihydrate and thiourea were set to a ratio of 1:1 and placed in 60 mL of hexamethylenetetramine for 30 min under stirring. Electrochemical reduction was performed at 0.5 V relative to the reversible hydrogen electrode (RHE). Reduction was completed when the cathodic current reached zero. Electrodeposition of CdS was accomplished in a three-electrode process using the Ni foam as working electrode, Ag/AgCl as counter electrode, and pure platinum as reference electrode. A potential of 1.0 V and an electrodeposition time of 70 s were applied relative to the RHE to control the CdS content. Then, the sample was washed with deionized water and left to dry at room temperature.

As for the shell, 25 mM of cobalt(II) nitrate hexahydrate, 25 mM of nickel(II) nitrate hexahydrate, and 25 mM of hexamethylenetetramine (as a hydrolyzing agent) were kept in 100 mL of deionized water for 30 min under stirring. The Ni foam on whose surface CdS nanowires had grown was placed in the autoclave. Subsequently, the prepared transparent solution (described above) was added to the autoclave, which was then tightly closed before being placed in an oven at 220 °C for 16 h. Lastly, the 3-D CdS@NiCo-LDH/NF core-shell electrode was removed from the autoclave, slowly washed with deionized water, and left to dry in room temperature.

2.3. Materials characteristics

The structure and crystal morphology of the sample were characterized via scanning electron microscopy (SEM) (model: SU8010; CRMD, USA), high-resolution transmission electron microscopy (HR-TEM) (model: Model JEM-2100 JEOL, Japan), X-ray photoelectron spectroscopy (XPS) (model: Kratos Analytical Ltd., Manchester, UK), and inductively coupled plasma mass spectrometry (ICP-MS) (model: NexION 300×, Perkin Elmer, USA). Surface areas were determined through Brunauer-Emmett-Teller (BET) measurements (Micromeritics apparatus ASAP 2020 M). The phase composition of the sample was characterized through X-ray diffraction (XRD) (Bruker D8 Advance X-ray diffractometer fitted with Cu Kα radiation). The amount of oxygen produced in the gas phase was monitored through the use of an online gas chromatograph (GC7900, Tian Mei, Shanghai). Photoluminescence spectra were obtained using FLS980 Edinburgh Instruments.

2.4. Electrochemical measurements

Electrochemical measurements were performed at an electrochemical unit (SP 150 Gill; ec-lab, UK) in a standard system consisting of three electrodes: the CdS@NiCo-LDH sample used as working electrode, Ag/AgCl electrode used as reference electrode, and pure platinum used as counter electrode. The OER and HER activity was assessed drawing upon linear sweep voltammetry at a speed of 1 mV/s and chronopotentiometry at the current densities of 10, 100, 500, and 1000 mA cm⁻² in a 1 M electrolyte of potassium hydroxide saturated with oxygen.

Using the Nernst equation, E (V vs. RHE) = E (V vs. Ag/AgCl) + 0.197 V + 0.059 pH, all the potentials measured relative to the reference electrode were changed into the RHE. All the curves are

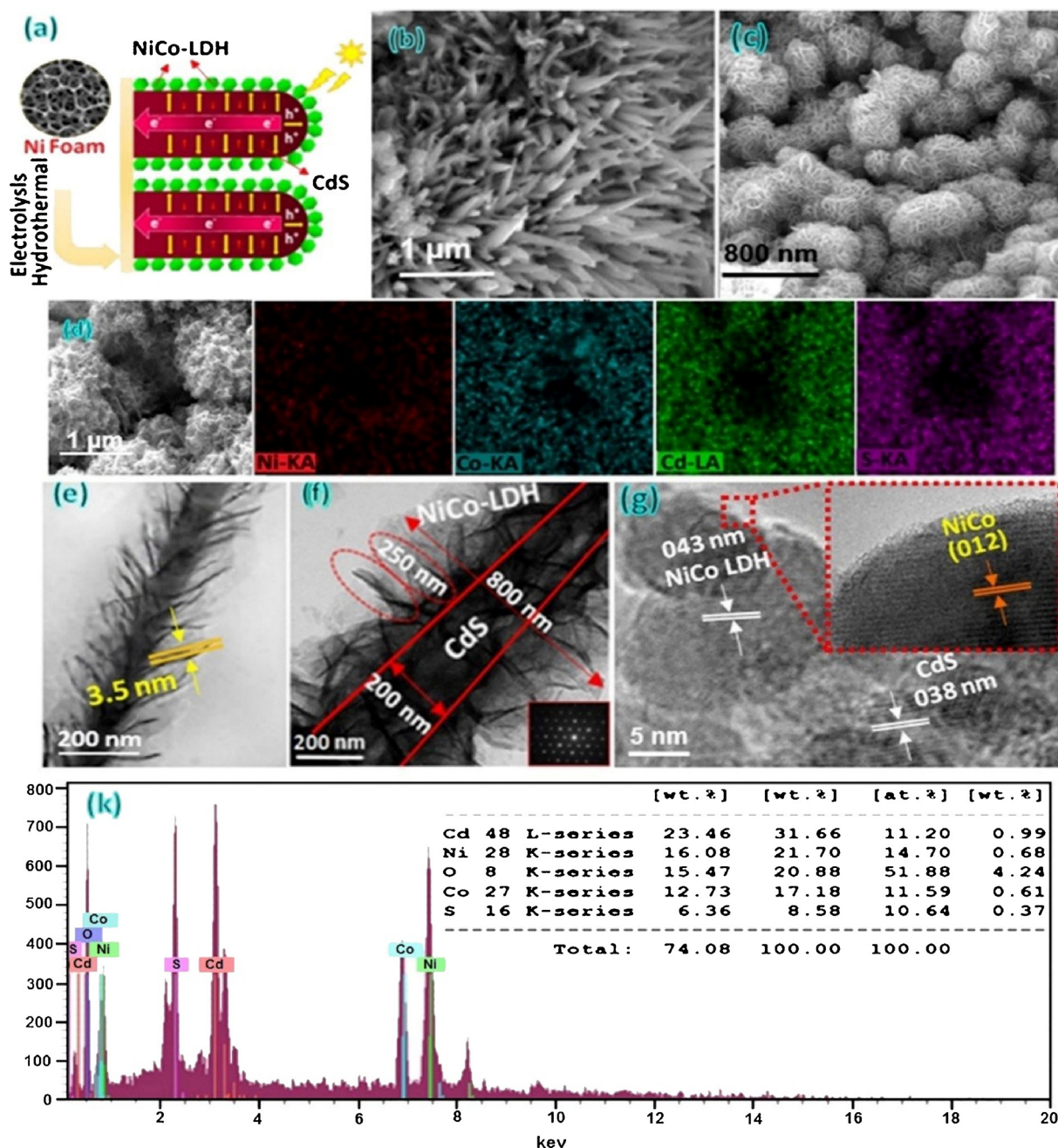


Fig. 1. Morphology and structural features: (a) schematic representation of a CdS@NiCo-LDH electrode in a nickel foam bed; (b) SEM images of CdS nanowires; (c) CdS@NiCo-LDH nanosheets; (d) elemental mapping analysis of the 3-D CdS@NiCo-LDH electrode; (e–g) HR-TEM images of the CdS@NiCo-LDH; (h) EDS spectra obtained from CdS@NiCo-LDH in (d).

reported via dynamic measurement.

3. Results and discussion

3.1. Characterization

Fig. 1 shows the process of synthesizing the CdS@NiCo-LDH photoelectrocatalyst. The Ni foam was employed as a substrate. Then, CdS nanowires were initially synthesized by means of direct electrochemical deposition, which is a compact, reliable, and low-cost method. Ultimately, thin films of NiCo-LDH were grown on CdS nanowires, resulting in the production of a 3-D CdS@NiCo-LDH catalyst.

Fig. 1(a) is the schematic representation of a CdS@NiCo-LDH electrode on the nickel foam. It also shows the SEM image of the 3-D porous

structure of the Ni foam with a soft surface full of grain boundaries. Fig. 1(b) shows the growth of dense and almost vertical nanowires on the Ni foam substrate after the electrochemical deposition of CdS. Fig. 1(c) is the SEM image of CdS@NiCo-LDH at high magnification and represents a 3-D macro-porous structure coated with uniform nano-materials. Fig. 1(d) illustrates the elemental mapping analysis and indicates an important point about the structure of the core-shell, which is clearly nickel as the bed, and nickel, cobalt, cadmium, and sulfur all distributed uniformly throughout the composite. The HR-TEM images in Fig. 1(e) display nanosheets grown on CdS nanowires, which has led to the formation of a surface with many pores that provide many channels for the penetration of electrolyte and the release of oxygen and hydrogen [27]. As shown in this figure, NiCo-LDH is about 3.5 nm thick. Fig. 1(f) more closely illustrates the HR-TEM image of a hybrid

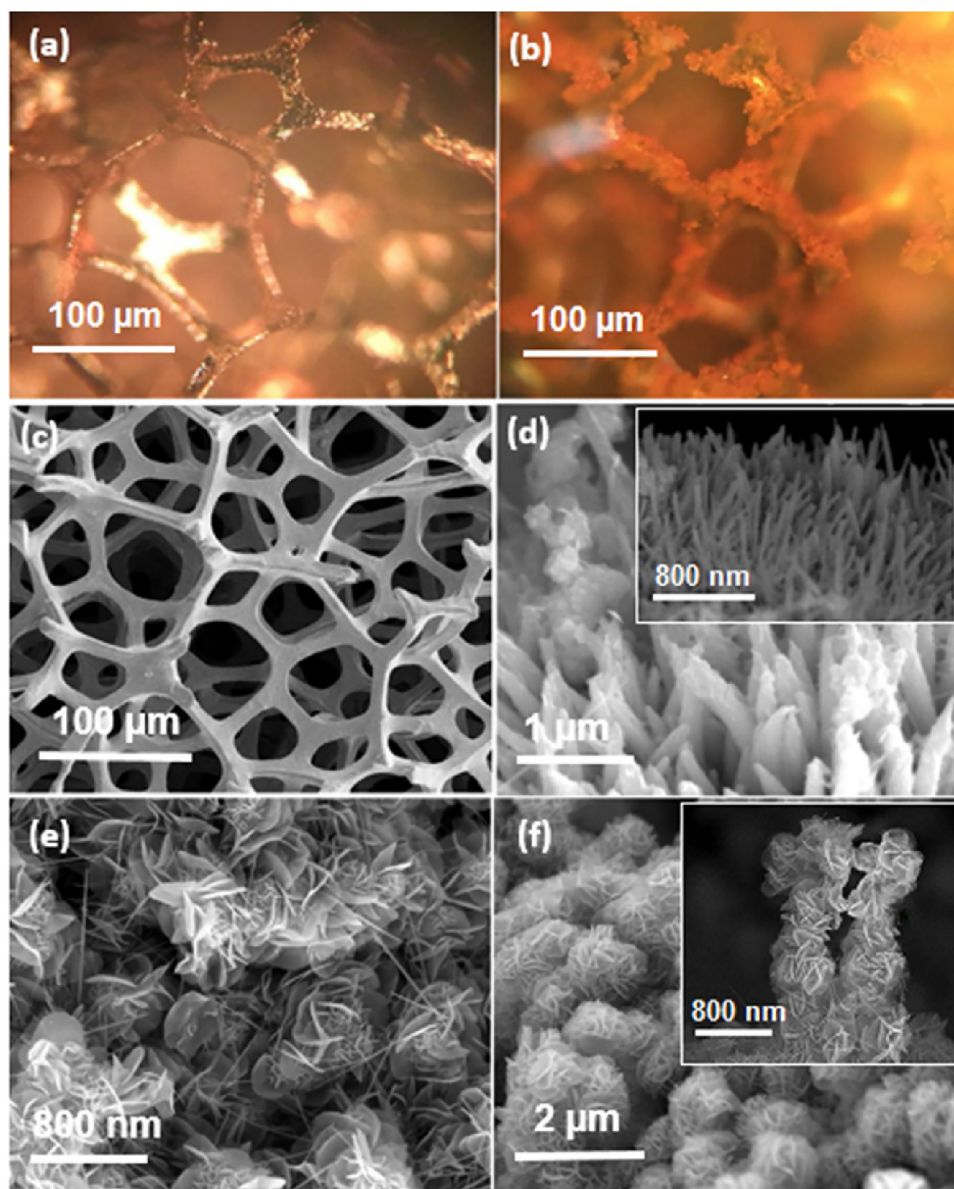


Fig. 2. Optical microscopy image of (a) Ni foam and (b) CdS@NiCo-LDH/NF; (c) SEM image of the porous Ni foam; (d–f) the growth of LDH sheets on CdS nanowires over time; the insets in Fig. 2(d) and (f) shows a cross-section of the CdS nanowire and the growth of LDH sheets on one CdS nanowire, respectively.

nanostructure, where CdS@NiCo-LDH has grown vertically on the Ni foam. As can be seen, the diameter of the core-shell is about 800 nm, the core of the CdS nanowires measures 200 nm, and the NiCo-LDH shell is 250 nm. Since an LDH layer is approximately 0.8 nm in thickness [28], the NiCo sample has an LDH of about 4 or 5 layers. A 3-D core-shell nanostructure with many NiCo-LDH layers maximizes the specific surface area and exposes more active corners to water molecules, thereby improving the catalytic activity. As Fig. 1(g) depicts, separate layers have an internal sheet spacing of 0.43 nm, which is related to the NiCo-LDH sheet (i.e., 012). Internal sheet spacing in another part of Fig. 1(g) is 0.38 nm, which is related to CdS. Moreover, the EDS data (Fig. 1k) demonstrate the existence of nickel, cobalt, cadmium, sulfur, and oxygen, denoting that the CdS@NiCo-LDH composite material was synthesized successfully.

ICP-MS has a number of advantages, such as the capability of performing simultaneous multi-element measurements together with very low limits of detection and a greater linear dynamic range. For the synthesized sample, the Cd:S:Ni:Co ratio was determined to be 0.51:0.19:0.44:0.53, giving a stoichiometric formula of

$\text{Cd}_{0.19}\text{S}_{0.21}\text{Co}_{0.27}\text{Ni}_{0.33}$. CdS@NiCo-LDH, CdS, and NiCo had roughly the same BET surface: 13.22, 8.54, and 12.78 $\text{m}^2 \text{g}^{-1}$, respectively.

Fig. 2(a) and (b) are images of the Ni foam and the CdS@NiCo-LDH from an optical microscope. As can be seen, CdS@NiCo-LDH is directly synthesized on the Ni foam with a porous structure, a wide active area, and a high electrical conduction [27]. The Ni foam has micro holes and zigzag flow channels within it that allow superior mass transfer and a large surface area per unit area [27]. The direct growth of LDH sheets on the Ni foam increases contact between the catalyst and the substrate to transfer electrons over time during overall water splitting reactions. In addition, the bubbles produced in water splitting tend to accumulate under planar substrates, and this causes overpotential at high current densities [29]. Fig. 2(c) shows the porous structure of the Ni foam, and Fig. 2(d), (e), and (f) depict the growth of LDH sheets on CdS nanowires after 2, 4, and 6 h of hydrothermal process, respectively. It is evident that the growth and concentration of LDH sheets increases with the passage of time. An increase in the concentration of LDH sheets leads to the generation of active sites and an increase in the number of electron-holes and enhances electron transfer on the surface of the NiCo-LDH

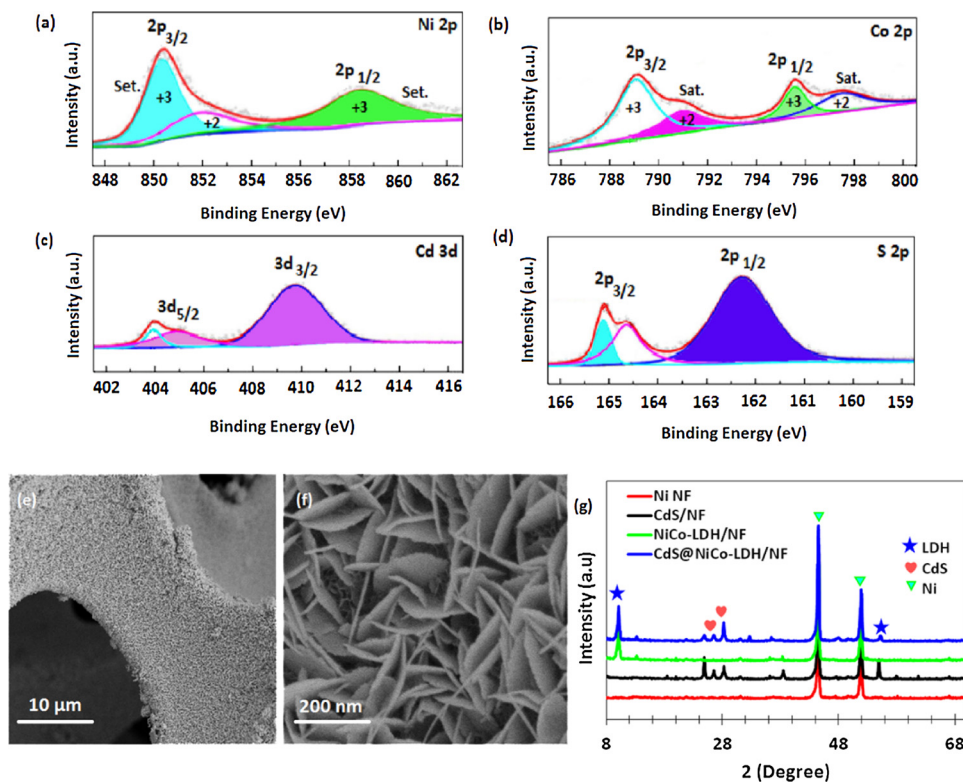


Fig. 3. (a–d) XPS graphs of Ni 2p, Co 2p, Cd 3d, and S 2p; (e–f) SEM images of NiCo-LDH nanosheets on the surface of the Ni foam; (g) XRD spectra of the Ni foam, CdS nanowires, NiCo-LDH, and CdS@NiCo-LDH.

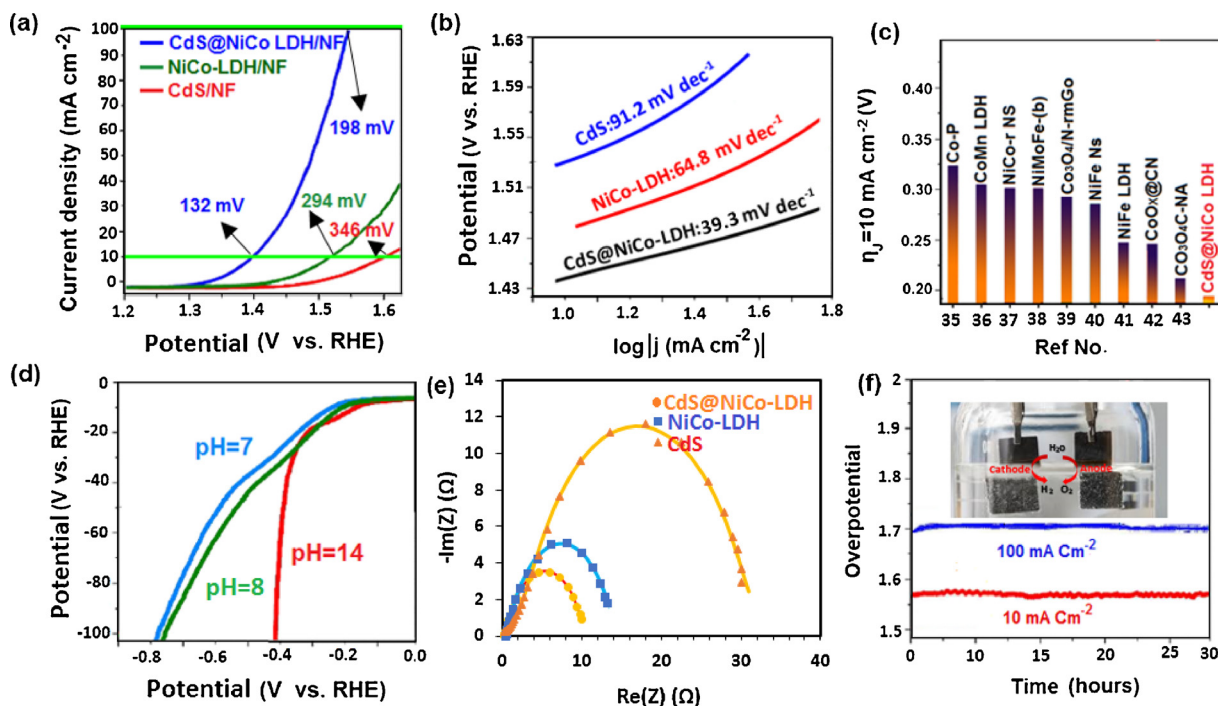


Fig. 4. The OER process of the CdS@NiCo-LDH core-shell in one Molar potassium hydroxide: (a) polarization graphs; (b) Tafel plots of as-prepared samples; (c) comparison between the needed overpotential at 10 mA cm⁻² and the Tafel slope with other high-performance electrocatalytic agents recently reported; (d) HER activity at different pH levels; (e) Nyquist plots of the samples examined at an overpotential of 250 mV; (f) chronopotentiometry graphs of core-shell at a continuous current density of 10 and 100 mA cm⁻².

shell.

The XPS test was performed for elemental and chemical bonding analysis of CdS@NiCo-LDH. Fig. 3(a–d) shows the signals of nickel, cobalt, cadmium, and sulfur. In addition to the shake-up satellites

characterizing the mixed valence of Ni²⁺/Ni³⁺ and Co²⁺/Co³⁺, Ni 2p and Co 2p spectra were fitted with two spin-orbit doublets. We observe in Fig. 3(a) that the binding energy of Ni 2p_{3/2} was decomposed to 850 and 852 eV, revealing the presence of Ni²⁺ and Ni³⁺ oxidation state

Table 1

Comparison of the OER and HER performance of the CdS@NiCo-LDH catalyst and other reported photoelectrocatalysts in a one Molar alkaline electrolyte (KOH). Here, η_{-5} , η_{-10} , and η_{-100} correspond to overpotentials at the current densities of 10 and 100 mA cm⁻² for OER and HER, respectively.

Catalyst	Support	η for OER - corresponding j (mV@ mA cm ⁻²)	Tafel slope (mV dec ⁻¹)	η for HER - corresponding j (mV@ mA cm ⁻²)	Tafel slope (mV dec ⁻¹)	Reference
FeNi ₃ N	Ni foam	202@100	40	75@10	98	[47]
Ni ₃ N/CMFs/ Ni ₃ N	Ni foam	115@10	52.1	270@10	41.5	[48]
NF-Ni ₃ Se ₂	NW/CC	353@100	–	79@100	97	[49]
FeNi ₃ N	Ni foam	202@100	40	75@10	86	[50]
NiMoP ₂ NW/CC	Glass carbon	320@20	90.6	199@100	112	[51]
NiCoP	Ni foam	32@10	37	280@10	87	[52]
(Co _{1-x} Fe _x) ₂ P	P-Ni foam	1.53@10	30	64@10	45	[53]
CoP NS@MW	Ni foam	–	–	296@100	96	[54]
Fe(TCNQ) ₂	Fe foil	340@10	110	–	–	[55]
Ni/Mo ₂ C-PC	Glass carbon	1.66@10	–	179@10	101	[56]
N,S-CNT	Glass carbon	360@10	56	170@5	133	[57]
Co-CuO NA	Cu foam	330@100	–	–	–	[58]
CdS@NiCo-LDH	Ni foam	198@100	39.3	202@100	41,3	The present study

with a Ni²⁺/Ni³⁺ atomic ratio of 0.9 on the basis of the integral peak area [30]. Moreover, the peak of Ni 2p_{1/2}, appearing at 858 eV, corresponds to Ni³⁺. Fig. 3(b) indicates that the binding energy of Co 2p_{3/2} was broken up into 789.2 and 791 eV, showing the presence of Co²⁺ and Co³⁺ oxidation state with a Co²⁺/Co³⁺ atomic ratio of 0.9 based on the integral peak area [21]. Furthermore, the peaks of Co 2p_{1/2}, located at 795.5 and 797.4 eV, are related to Co³⁺ and Co²⁺, respectively. In Fig. 3(c), the binding energies of Cd 3d_{5/2} and Cd 3d_{3/2} are observed at 404 and 409.7 eV, respectively. In addition, the presence of Cd²⁺ on the surface of CdS nanowires is indicated in a spin energy separation of 5.8 eV between Cd 3d_{3/2} and Cd 3d_{5/2} [31]. Another point worth noting is the shifting of both the Cd 3d_{3/2} and Cd 3d_{5/2} peaks from their standard location (412.2 and 405.1 eV, respectively) [32] to higher energy levels (409.7 and 404 eV, respectively), together with a significant decline in the height as a result of interaction between the CdS core and the NiCo-LDH shell [21]. In Fig. 3(d), the peaks at 163.5 and 165 eV are attributable to the characteristic peaks of the S 2p_{1/2} and S 2p_{3/2} spin-orbit components of S²⁻. This suggests that S²⁻ is the main form existing on the surface of CdS nanowires [33].

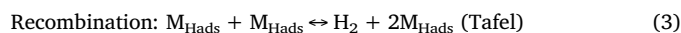
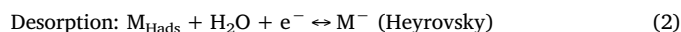
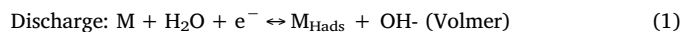
For comparison purposes, NiCo-LDH was grown on the same Ni foam under the same experimental conditions, with SEM images being shown in Fig. 3(e–f). Fig. 3(f), which is a higher magnification of Fig. 3(e), shows that NiCo sheets are homogenous and that very thin LDH sheets have grown compactly on the Ni foam.

Then, the XRD test was performed to identify the phases of the sample. Fig. 3(g) shows two sharp peaks at 44.34 and 53.58 at 2 θ angle, which are related to the cubic structure of nickel. The image shows phase transition from CdS to LDH and the high crystallization of the composite. This method can easily give us enough information for the synthesis of advanced LDH core-shell semiconductors [34].

The OER activities of the CdS, NiCo-LDH, and CdS@NiCo-LDH electrodes at current densities of 10 and 100 mA cm⁻² were studied in 1 M potassium hydroxide, with the results depicted in Fig. 4.

The polarization curves in Fig. 4(a) shows that CdS@NiCo-LDH has much more activity than either CdS or NiCo-LDH. In particular, this CdS@NiCo-LDH core-shell can produce current densities of 10 and 100 mA cm⁻² at overpotentials of 132 and 198 mV, respectively. As for NiCo-LDH and CdS, to generate a current density of 10 and 100 mA cm⁻², an overpotential of 294 mV and 346 mV are required, respectively. It was found that there is very little overpotential with the CdS@NiCo-LDH electrode, which is much better than the other two electrodes mentioned. Fig. 4(b) demonstrates that the CdS@NiCo-LDH electrode has a minor Tafel slope of 39.3 mV/dec, which shows excellent OER performance compared to the two other catalysts under study. Fig. 4(c) strongly suggests that the CdS@NiCo-LDH 3-D core-shell electrode, which is the OER catalyst, is very efficient and performs better than the competing electrodes at issue, especially at high current

density levels [35–43]. As it is clear in Fig. 4(d), the CdS@NiCo-LDH 3-D core-shell HER electrode shows superior catalytic activity with great stability (maintaining catalytic activity at all alkaline pH levels). This can be attributed to the superaerophobic surface, the direct and fast transfer of electrons from CdS@NiCo-LDH to the Ni foam, and strong chemical composition between CdS@NiCo-LDH core-shell and the Ni foam substrate. Cathodic HER in alkaline water electrolysis goes through the following reaction steps (Eq. (1) to (3)) [44]:



where the adsorbed hydrogen atom (H_{ads}) undergoes a reaction with water molecules to generate H₂ and to release hydroxides [45]. Both pathways entail the adsorption of the water molecule, dissociation of adsorbed water molecules into adsorbed hydrogen and hydroxides, desorption of hydroxides to revive the surface, and transformation of adsorbed H into H₂ [44].

To investigate the kinetics of the electrodes, electrochemical impedance spectroscopy (EIS) was used. Fig. 4(e) shows that the 3-D electrode has a considerably low charge transfer resistance (R_{ct}) of about 7.2 Ω , as opposed to pure NiCo LDH (9.1 Ω) and the CdS nanowire (12.68 Ω). Vertically positioning the electrodes near one another will lower the ohmic resistance between them. Furthermore, the use of highly active metals and porous materials will improve the electrical and ionic conductivity of the system [27]. Forcing the gas (i.e., hydrogen and oxygen) bubbles to disengage from the electrode and separator surfaces and to quit the system will decrease the formation of void fraction, reduce the impedance, and improve efficiency [46].

The lower R_{ct} indicates that electron transfer and catalyst kinetics are desirable, resulting in a small Tafel slope. Low R_{ct} may be due to these causes: (1) CdS nanowires are synthesized on the Ni foam and are strongly attached to NiCo-LDH, increasing the surface and providing more active sites for photocatalytic reactions [10]; (2) the 3-D NiCo-LDH structure allows the penetration of water molecules, leading to a convenient contact between the CdS@NiCo-LDH core-shell and the electrolyte. Furthermore, the internal sheet gap between the layers is suitable for the release of gaseous products; and (3) the unique 3-D core-shell structure can provide more surfaces with more accessible active sites, permitting the gaseous products to release rapidly [46]. In addition, this structure expedites the transfer of electrons from the Ni foam to CdS nanowires and then to the external shell of the NiCo-LDH layer.

As shown in Fig. 4(f), overpotential causes the current densities of 10 and 100 mA cm⁻², which apparently do not enhance during a 30-hour-long period. It should be noted that the little change observed in

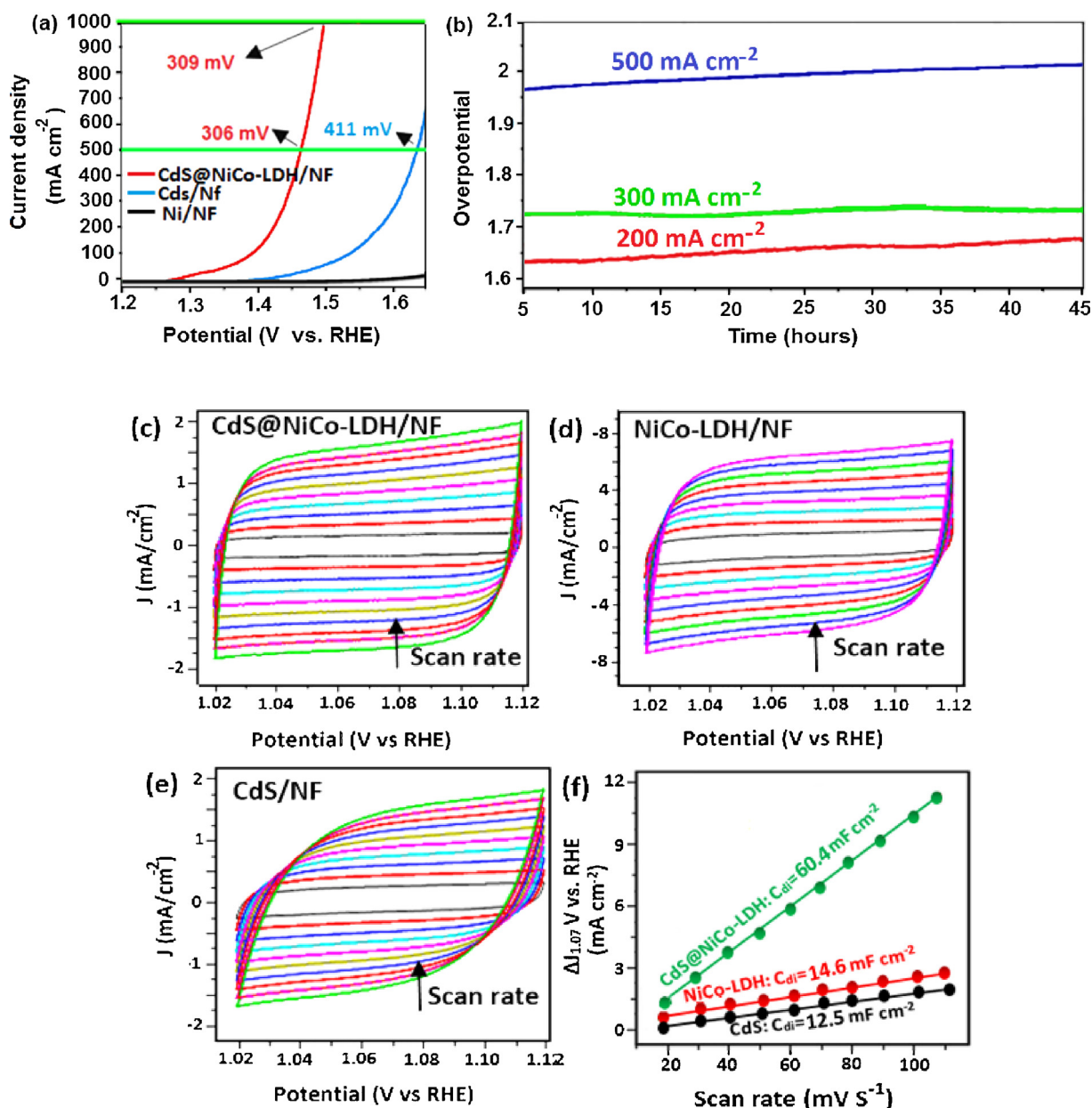


Fig. 5. The OER process of CdS@NiCo-LDH in one Molar potassium hydroxide: (a) polarization graph at current densities of 500 and 1000 mA cm⁻²; (b) chronopotentiometry curves of CdS@NiCo-LDH at constant current densities of 200, 300, and 500 mA cm⁻². Typical cyclic voltammograms at scan rates with the potential range of 1.025–1.125 V vs. RHE; (c) CdS@NiCo-LDH; (d) NiCo-LDH; (e) CdS nanowires; (f) capacitive currents representing a function of the scan rate.

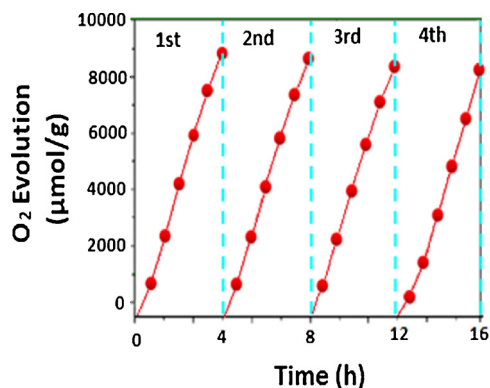


Fig. 6. Stability tests of OER for CdS@NiCo-LDH.

this figure is due to the fact that the long-term stability test is a dynamic process and the contributing factors, such as the absorption of bubbles on electrodes surface, cause potential changes.

Table 1 provides the detailed results of the comparison of the proposed CdS@NiCo-LDH and other recently reported catalysts in terms of OER and HER performance in alkaline environments. It can be seen that our 3-D CdS@NiCo-LDH acts better than the alternative catalysts based on non-noble metals.

The OER performance of the CdS, NiCo-LDH, and CdS@NiCo-LDH electrodes at current densities of 500 and 1000 mA cm⁻² were explored in 1 M potassium hydroxide (Fig. 5).

Fig. 5(a) shows that CdS@NiCo-LDH can generate current densities of 500 and 1000 mA cm⁻² at overpotentials of 306 and 309 mV. As for CdS on the Ni foam, an overpotential of 411 mV is needed to generate a current density of 500 mA cm⁻². It was observed that overpotential with the CdS@NiCo-LDH electrode is very little, which is much better than in the case of the other electrodes under comparison.

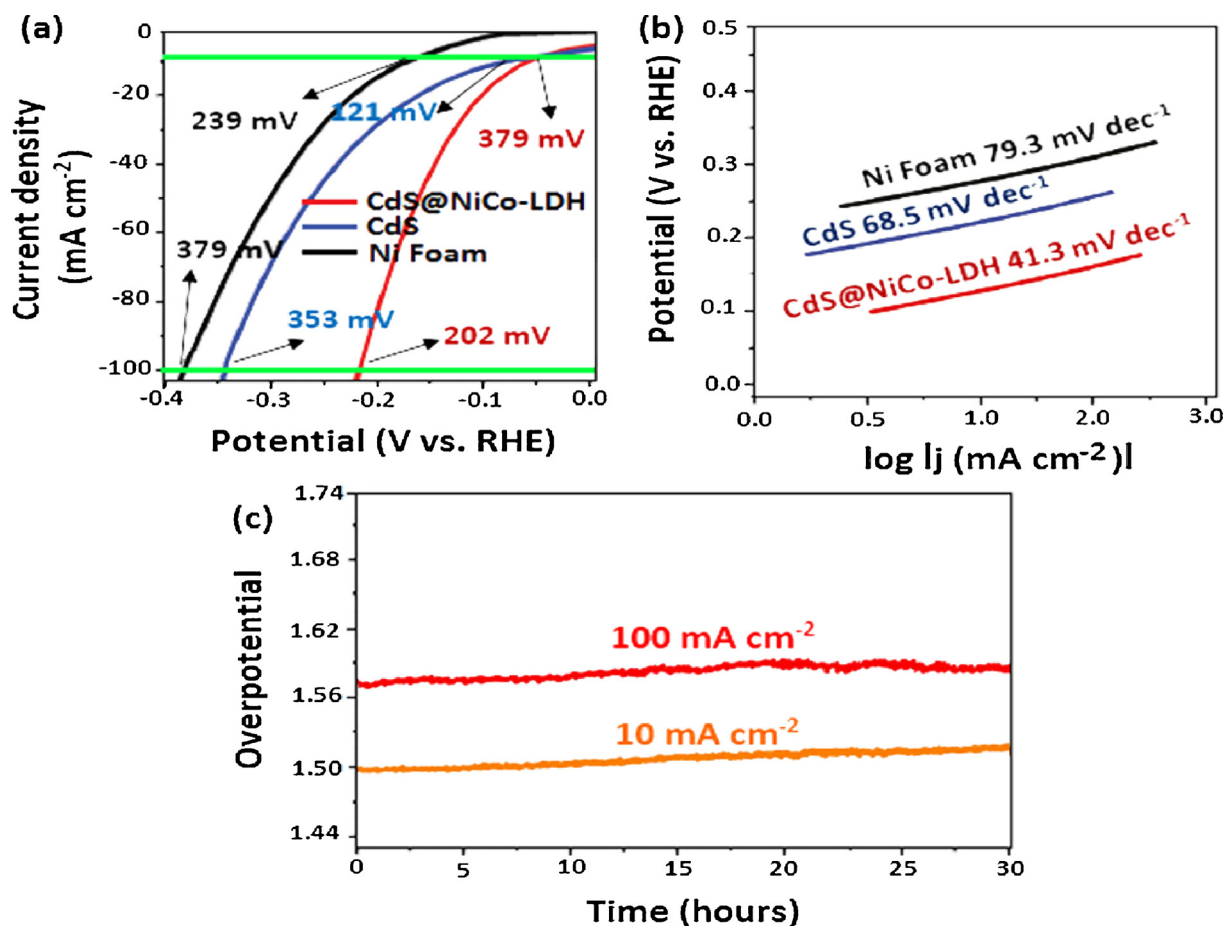


Fig. 7. The HER process of CdS@NiCo-LDH in one Molar potassium hydroxide: (a) polarization graph at current densities of 10 and 100 mA cm^{-2} ; (b) corresponding Tafel plots; (c) Time parameter of the current density for CdS@NiCo-LDH under a constant condition of overpotential of 180 mV allowed a current density of 30 mA.

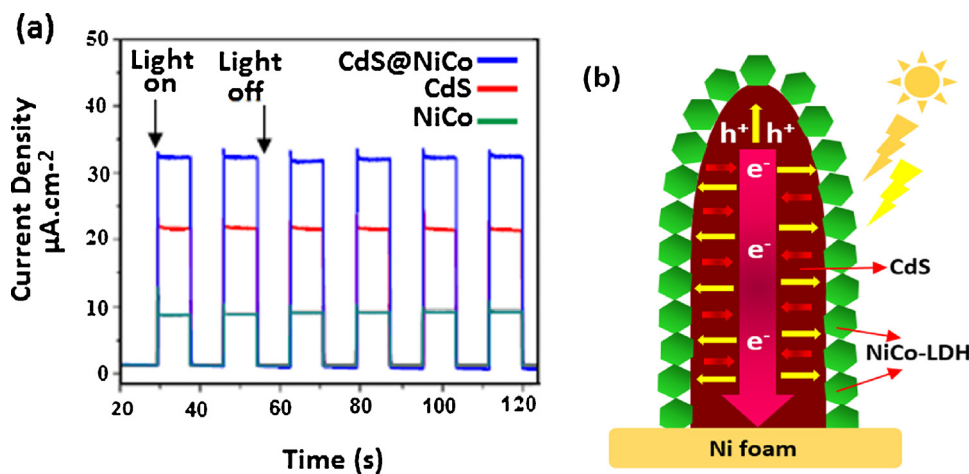


Fig. 8. (a) Photocurrent density-time ($I-t$) response of pure CdS, NiCo-LDH, and CdS@NiCo-LDH under visible light irradiation; (b) charge transfer from CdS@NiCo-LDH to water through Ni foam.

As can be seen in Fig. 5(b), overpotential leads to the current densities of 200, 300, and 500 mA cm^{-2} , which seemingly do not enhance during a period of 45 h. CdS nanowires that have grown on the Ni foam and tightly attached to NiCo-LDH are indicative of a good electrical contact and good mechanical stability. A gradual increase can be seen at 200 and 500 mA cm^{-2} , which is attributable to the accumulation of gas bubbles in the porous electrode, leading to a reduced rate of the outflow of gas from the electrode [59].

Fig. 5(c) and (e) shows the typical cyclic voltammograms used to

calculate the double-layer capacitance of the two electrodes being studied. The double-layer capacitance (C_{dl}) was calculated via plotting $\Delta J (J_a - J_c)$ at 0.95 V against the scan rate. In this formula, J_a and J_c are the anodic and cathodic current density, respectively, and the slope is twice as large as C_{dl} [60,61]. According to Fig. 5(f), the double-layer capacitance ($60.4 \mu\text{F cm}^{-2}$) shown by the CdS@NiCo-LDH electrode is proportionate to the active electrochemical surface. This value is higher than the corresponding values of pure NiCo-LDH ($14.6 \mu\text{F cm}^{-2}$) and the CdS nanowire ($12.5 \mu\text{F cm}^{-2}$).

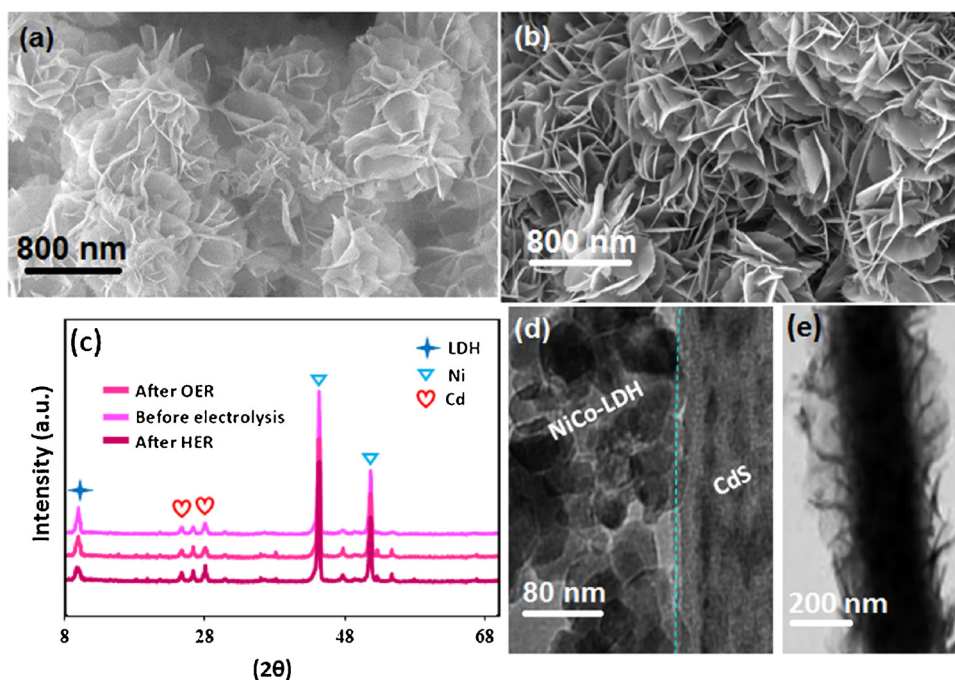


Fig. 9. (a) SEM of the CdS@NiCo-LDH electrophotocatalyst after OER electrolysis, (b) SEM of CdS@NiCo-LDH after HER electrolysis, (c) XRD before and after OER/HER electrolysis, (d) TEM following OER electrolysis, and (e) TEM subsequent to HER electrolysis.

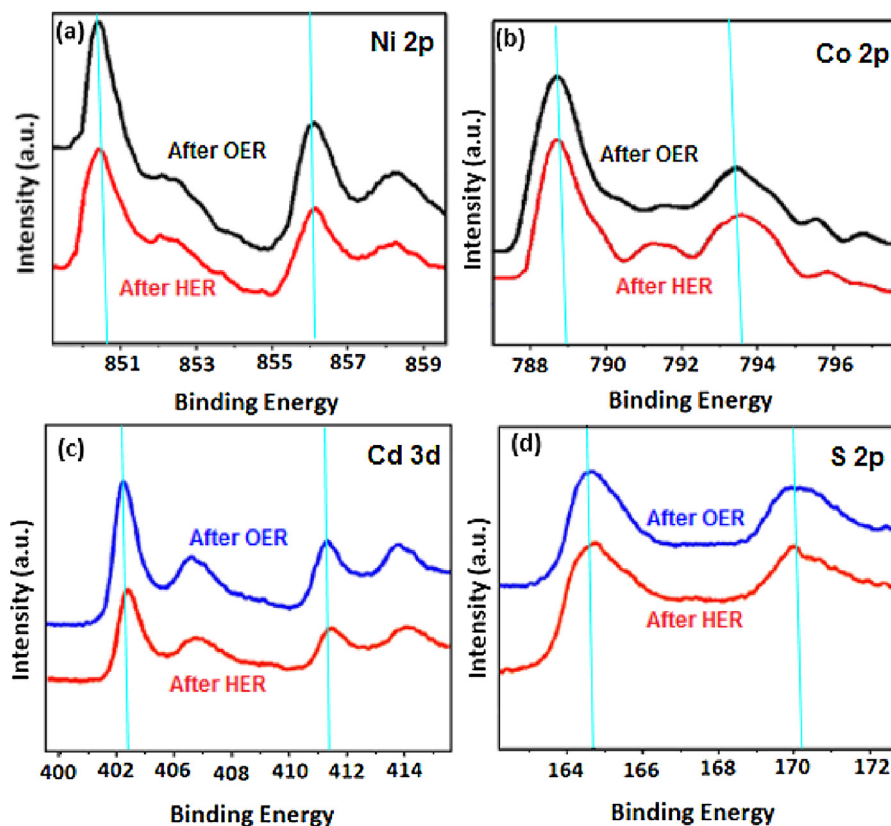


Fig. 10. (a–d) XPS graphs of Ni 2p, Co 2p, Cd 3d, and S 2p of the CdS@NiCo-LDH electrophotocatalyst after OER /HER electrolysis.

Fig. 6 illustrates the results from stability tests of OER performed on the CdS@NiCo-LDH photoelectrocatalyst. The minimal increase in the amount of OER in the third cycle can be put down to the transfer methods employed by carriers in the CdS@NiCo-LDH nanostructure. The many LDH sheets appearing on the surface of the CdS@NiCo-LDH catalyst create many sites that trap water molecules. This efficiently

transfers electrons from the inside to the surface, thereby bringing about enhanced photocatalytic HER [62]. It can be seen that the CdS@NiCo-LDH catalyst shows great stability throughout the four cycles, with the maximum amount of OER being $9000 \mu\text{mol g}^{-1}$.

The total oxygen production detected by a gas chromatograph. The red lines are the theoretical oxygen production calculated from the

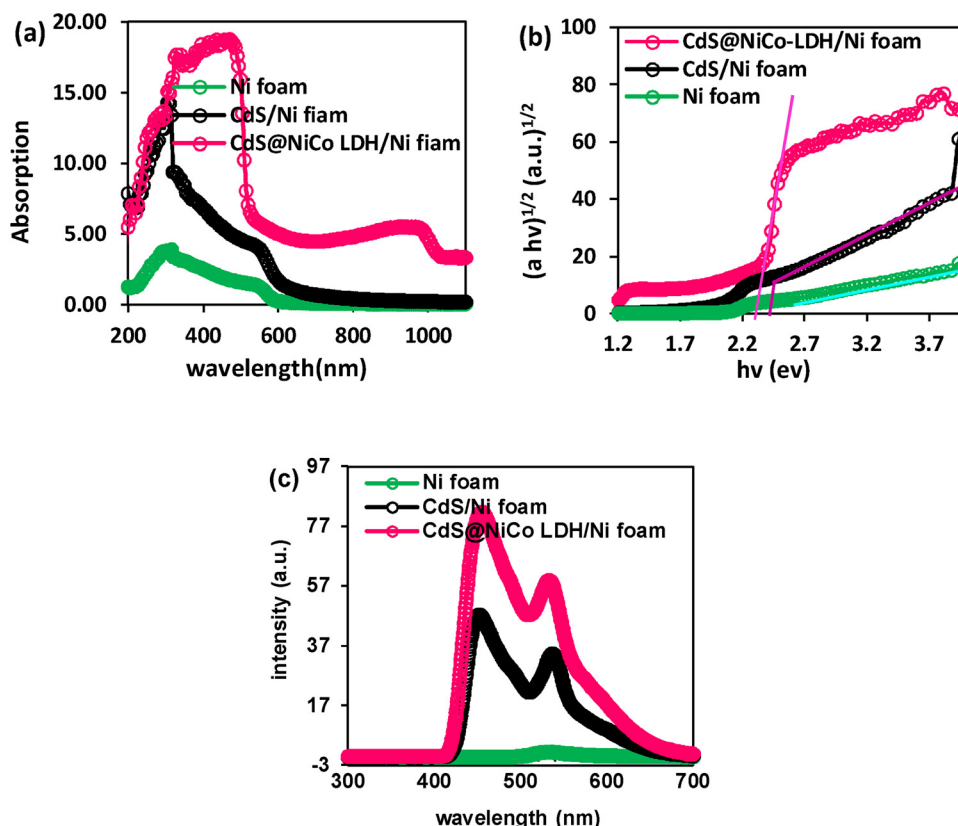


Fig. 11. (a) UV-vis diffuse-reflectance spectra of CdS@NiCo-LDH, CdS/NF, and the Ni foam; (b) the corresponding plots of $(ah\nu)^{1/2}$ vs. $h\nu$ (a = absorption coefficient) employed to determine the band gap energy of CdS and CdS@NiCo-LDH; (c) photoluminescence spectra of CdS@NiCo-LDH, CdS/NF, and the Ni foam.

measured photocurrent on the assumption of a faradaic efficiency of 100%. The total oxygen production includes the amount of oxygen in the headspace calculated using the ideal gas law and the oxygen dissolved in the electrolyte calculated following the Henry's law.

The electrocatalytic ability of the CdS@NiCo-LDH photoelectrocatalyst for HER was also measured in one Molar potassium hydroxide to examine water splitting. The polarization curves in Fig. 7(a) indicate that CdS@NiCo-LDH has considerably more activity than either CdS/NF or the Ni foam. Particularly, this CdS@NiCo-LDH can generate current densities of 10 and 100 mA cm⁻² at overpotentials of 379 and 202 mV, respectively. As for CdS, to produce a current density of 10 mA cm⁻², an overpotential of 121 mV and 353 mV are required, respectively. Fig. 7(b) indicates that the CdS@NiCo-LDH electrode has a very small Tafel slope of 41.3 mV/dec, implying excellent HER performance compared to the other photoelectrocatalysts under comparison.

As shown in Fig. 7(c), overpotential results in the current densities of 10, and 100 mA cm⁻², which did not improve during a period of 30 h. CdS nanowires that have grown on the Ni foam and closely attached to NiCo-LDH indicate a good electrical contact and great mechanical stability.

Fig. 8 shows the photoelectron chemical measurements performed on the samples to explore the temporary photocurrent responses of the CdS@NiCo-LDH, CdS, and NiCo electrodes. For all the samples, upon irradiation at (AM 1.5, 100 mW cm⁻², and bias voltage of 0.1 V vs. Ag/AgCl), a surge was seen in the photoresponse because of the transitory impact in power excitation, and then the photocurrent swiftly reached the steady state. CdS@NiCo-LDH was found to exhibit the highest degree of photocurrent density, which quickly approached zero in the absence of visible light, an observation ascribable to the rapid transfer of photo-produced electrons from the CdS core to the NiCo-LDH shell. These findings indicate that the CdS@NiCo-LDH photoelectrode shows excellent electrocatalytic performance. Fig. 8(b) is the scheme of

electrons transfer. The evolution of hydrogen and oxygen under UV-vis on pure CdS is accomplished due to a relatively narrow band gap (2.4 eV) and the position of conduction band (0.7 V) and the valence band (1.7 V) relative to the standard hydrogen electrode. The absorption of photons by CdS causes electron-hole pairs on the surface of CdS nanowires. Then, electrons transfer to the NiCo-LDH sheets, thereby causing active sites on the surface of the NiCo-LDH sheets and water oxidation. Furthermore, the coating of the NiCo-LDH sheets on CdS nanowires prevents photo corrosion of CdS.

Fig. 9(a) and (b) presents the SEM of the CdS@NiCo-LDH photoelectrocatalyst after OER and HER, respectively. These figures show that the sharp edges of the LDH sheets decreased and the distance between these sheets increased slightly. Using the Ni foam with big and open pores is a network for the growth of semi-conducting materials with a high density and the stable vertical growth of nano-structures, a fact which speeds up the transfer of electrons from the 3-D catalyst to the electrolyte and increases the distance between LDH sheets. Fig. 9(c) shows XRD prior to and following OER and HER electrolysis. The peaks at 10° are related to LDH sheets [63], and the peaks at 45° are concerned with the Ni; the peaks at 24°, 26°, and at 28° concern CdS [64]. Lastly, Fig. 9(d) and (e) shows the TEM of the CdS@NiCo-LDH subsequent to OER/HER electrolysis, respectively.

As displayed in Fig. 10 (a), the XPS spectrum of Ni 2p is well fitted with two chiral spin-orbits. Binding energy at 850.62 eV indicates Ni 2p_{3/2} OER /HER after the process. Moreover, the peak of Ni 2p_{1/2}, appearing at 856.25 eV, corresponds to Ni³⁺. According to Fig. 10b, the binding energies at 788.9 eV for Co 2p_{3/2} and 793.78 eV for Co 2p_{1/2} demonstrate the coexistence of Co²⁺ and Co³⁺. In the XPS spectrum of Cd 3d shown in Fig. 10c, the binding energies of Cd 3d_{5/2} and Cd 3d_{3/2} are 402.2 and 411.7 eV [32]. Peaks at 164.7 eV and 170.1 eV (Fig. 10d) are attributed to the S 2p_{3/2} and S 2p_{1/2} of S²⁻ [33]. The XPS test was performed on electrodes after 30 h of OER and HER process. A very small shift was observed in some of the peaks, which may be due to a

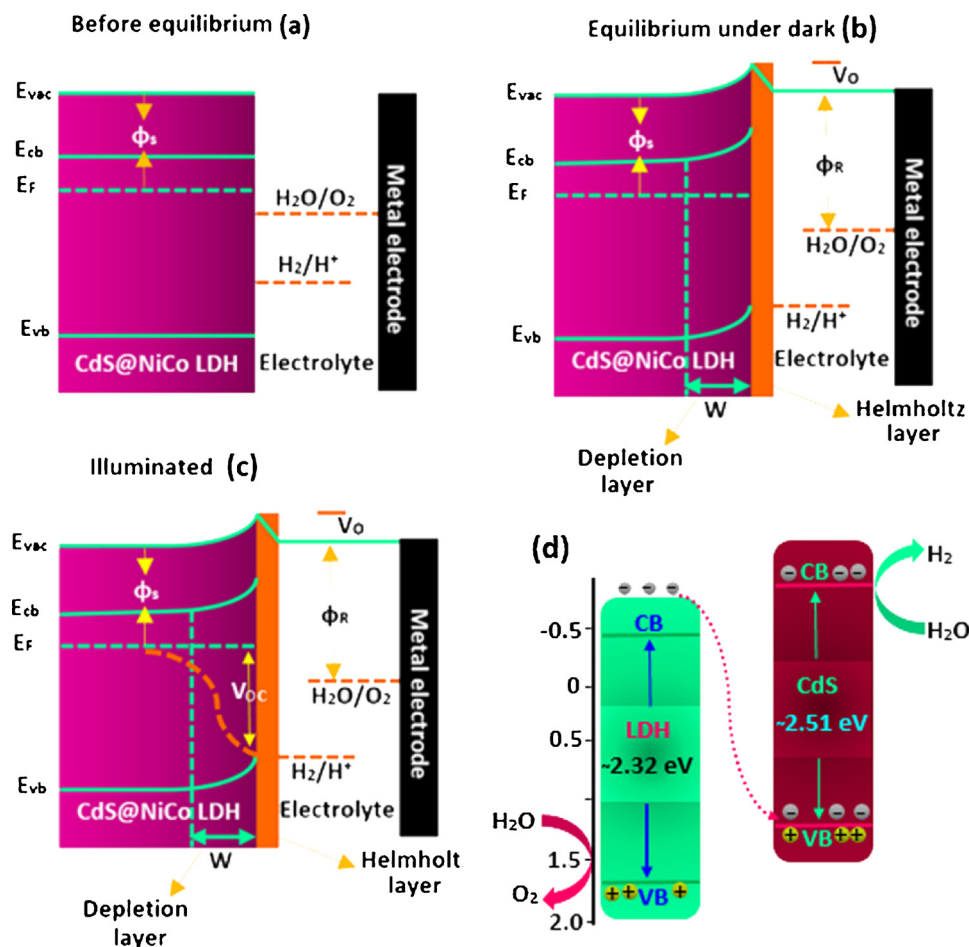


Fig. 12. The energy band of the bond between CdS@NiCo-LDH and the electrolyte represents the relationships between the Helmholtz layer potential drop and the redox electrolyte couple ($\text{H}_2\text{O}/\text{O}_2$ and H_2/H^+), (V_H), electrolyte work function (ϕ_R), electron quasi-Fermi level (E_{Fn}), hole quasi-Fermi level, semiconductor work function (ϕ_s), in three cases: (a) before the equilibrium between the two phases of electrode and electrolyte; (b) after the equilibrium in the absence of light; and (c) in the quasi-static equilibrium in the presence of irradiation. The open-circuit voltage (V_{OC}) produced by the junction in the presence of light conditions is presented by the gap between E_{Fn} and the electrochemical potential of $\text{H}_2\text{O}/\text{O}_2$ for n-type semiconductors and H_2/H^+ for p-type semiconductors; (d) estimated band positions of CdS and NiCo-LDH in 1 M KOH electrolytes.

slight change in the crystal lattice or two capacity ion conversion to three capacity and electron transmissions for water splitting.

Fig. 11(a) presents the UV-vis region spectra of CdS and NiCo electrodes. The CdS spectrum is characterized by a strong absorption below 400 nm, which is pertinent to the typical band gap of CdS. The CdS@NiCo-LDH spectrum is characterized by an absorption between 200 and 1100 nm, with a λ_{max} of about 450 nm for NiCo and an absorption of about 300–600 for CdS-NiCo-LDH. As it is clear in this figure, the growth of LDH sheets significantly impacts upon CdS absorption. Maximum absorption has to do with the diffusion of physical light (i.e., photon behavior) and, to some extent, with the interference resulting from the wavelength of the single-wavelength photon in thin films. As displayed in Fig. 11(b), the band gaps of CdS@NiCo-LDH, CdS/ Ni foam, and the Ni foam were calculated to be about 2.51, 2.32, and 2.71 eV, respectively. This redshift in the optical absorption of the specimens may be pertinent to their morphological and structural differences [65]. The narrow band gap of the CdS@NiCo-LDH sample can be put down to the fact that the photoexcitation of this sample led to the production of electron-hole pairs on catalytic surface via visible light radiation, which resulted in the stimulation of the chemical redox reactions. In addition, variations in the band gap may have to do with a different degree of absorption and transfer of electron-hole pairs, which may depend on the photocatalytic mechanism [64,65]. Fig. 11(c) portrays photoluminescence spectra of CdS@NiCo-LDH, CdS/ Ni foam, and the Ni foam. The CdS@NiCo-LDH and CdS/ Ni foam samples show a photoluminescence peak in the wavelength range of 400 to 700 nm, which can be attributed to a recombination of photo-generated load carriers in these samples [66]. Moreover, the transfer of electron-hole pairs between CdS and NiCo-LDH caused the height of the photoluminescence peaks to increase.

As shown in Fig. 12, the electrochemical potential of the area where a semiconductor is immersed in the electrolyte is different throughout the electrode-electrolyte interface. For the balance of this interface, the band bending of CdS@NiCo-LDH and transfer of electrons from one phase to another should occur. In a semiconductor-liquid junction (SCLJ), the chemical potential balance of electrons in CdS@NiCo-LDH (Fermi level) and the oxidation-reduction potential in potassium-hydroxide solution transfer the electrons throughout the SCLJ. Another specified region exists in CdS@NiCo-LDH, where charge is eliminated by this process of equilibrium. It is also worth noting that since the depletion layer is electrically neutral, it is called space charge region (SCR) or discharge layer since it is evacuated from most charge carriers. One of the key features of CdS@NiCo-LDH used in the PEC decomposition of water is the presence of an electrical field in the SCR, which is a place for band bending. In the case of solar devices used for water decomposition, the SCR and band bending contribute to the transfer and separation of e^- and h^+ generated by photons. Consequently, it is very important to understand the different band bending types in PEC systems. Band bending is caused by the contact between a semiconductor and a metal and leads to the formation of the SCR. From the description of the band bending of CdS@NiCo-LDH and the SCR, we can calculate the band energy of the CdS@NiCo-LDH / potassium hydroxide electrolyte surface before the equilibrium between the electrode and the electrolyte, after the quasi-static equilibrium in the presence of light, and equilibrium under dark conditions. As Fig. 12 illustrates, when a CdS@NiCo-LDH photoelectrode is immersed in a potassium hydroxide solution containing $\text{H}_2\text{O}/\text{O}_2$, electron transfer takes place between CdS@NiCo-LDH and the potassium hydroxide electrolyte until equilibrium is achieved. In addition, the electrode shows an excessive positive charge due to the ionized atoms in CdS@NiCo-LDH, and the

electrolyte exhibits a surplus of negative charge. The depletion layer with W width is extended by the positive charge. In a very narrow region, Helmholtz layer is stretched over between CdS@NiCo-LDH and the potassium hydroxide solution and the negative charge increases. (Fig. 12(a–b)). In Fig. 12(c), the steady-state illumination causes a non-equilibrium between e^- and h^+ populations that can be elaborated using the concept of the quasi-Fermi level. The quasi-Fermi level of e^- and h^+ in the presence of light causes electrochemical potential at one moment. An electrical field creates a gradient in CdS@NiCo-LDH that results in a current and voltage. The voltage produced in the semiconductor is called the open-circuit voltage (V_{OC}), determined by the potential difference between the quasi-Fermi levels of the e^- and h^+ under a non-current circuit. The highest generated current in the electrical field is called the short-circuit current density (J_{SC}), and therefore the maximum power point (mpp) is obtainable by multiplying the V_{OC} by the J_{SC} in the following equation [67]: $mpp = V_{OC} \times J_{SC}$.

The positions of the CB and the VB of the two catalyst components are given in Fig. 12(d). Since the VB of CdS is lower than the CB of NiCo-LDH in terms of position, the photoexcited electrons from the CB of NiCo-LDH transfer to the VB of CdS. This will neutralize the holes produced on CdS, which will thus inhibit oxidation and increase photocatalytic capability. This shows that CdS and NiCo-LDH can generate oxygen and hydrogen in water splitting [64].

4. Conclusion

We synthesized a 3-D CdS@NiCo-LDH photoelectrocatalyst as a cost effective, bi-functional, and efficient catalyst for water splitting. The production of CdS@NiCo-LDH creates a composite with a high specific surface area that accesses active sites and is desired for water molecules adsorption and catalytic reactions. In addition, the particular layered structure of CdS@NiCo-LDH is desirable for the penetration of water molecules into LDH sheets, releasing gaseous products and providing more catalyst surface to the electrolyte. Moreover, the CdS core provides active sites for electron transfer. The CdS@NiCo-LDH core-shell catalyst exhibits excellent efficiency in alkaline environments for water splitting. We believe that this method could be used to develop other catalysts based on transition metals.

References

- [1] Z.W. Seh, J. Kibsgaard, C.F. Dickens, I. Chorkendorff, J.K. Nørskov, T.F. Jaramillo, Combining theory and experiment in electrocatalysis: insights into materials design, *Science* 355 (2017) 4998–5009.
- [2] B. Weng, C.R. Grice, J. Ge, T. Poudel, X. Deng, Y. Yan, Barium bismuth niobate double perovskite/tungsten oxide nanosheet photoanode for high-performance photoelectrochemical water splitting, *Adv. Energy Mater.* 8 (2018) 1701655.
- [3] T. Liu, L. Xie, J. Yang, R. Kong, G. Du, A.M. Asiri, X. Sun, L. Chen, Self-standing CoP nanosheets array: a three-dimensional bifunctional catalyst electrode for overall water splitting in both neutral and alkaline media, *ChemElectroChem* 4 (2017) 1840–1845.
- [4] L. Yao, N. Zhang, Y. Wang, Y. Ni, D. Yanb, C. Hu, Facile formation of 2D $Co_2P@Co_3O_4$ microspheres through in-situ topotactic conversion and surface corrosion: Bifunctional electrocatalysts towards overall water splitting, *J. Power Sources* 374 (2018) 142–148.
- [5] Z. Pei, H. Li, Y. Huang, Q. Xue, Y. Huang, M. Zhu, Z. Wang, C. Zhi, Texturing in situ: N, S-enriched hierarchically porous carbon as a highly active reversible oxygen electrocatalyst, *Energy Environ. Sci.* 10 (2017) 742–749.
- [6] X. Ji, B. Liu, X. Ren, X. Shi, A.M. Asiri, X. Sun, P-doped Ag nanoparticles embedded in N-doped carbon nanoflake: An efficient electrocatalyst for the hydrogen evolution reaction, *Chem. Eng.* 4 (2018) 4499–4503.
- [7] J. Zhao, X. Li, G. Cui, X. Sun, Highly-active oxygen evolution electrocatalyzed by a Fe-doped $NiCr_2O_4$ nanoparticles film, *Chem. Commun.* 54 (2018) 5462–5465.
- [8] B. Weng, C.R. Grice, W. Meng, L. Guan, F. Xu, Y. Yu, C. Wang, D. Zhao, Y. Yan, MOF-derived CoWP@C Composite Nanowire Electrocatalyst for Efficient Water Splitting, *ACS Energy Lett.* 3 (6) (2018) 1434–1442.
- [9] Q. Liu, L. Xie, Z. Liu, G. Du, A.M. Asiri, X. Sun, Zn-doped Ni_3S_2 nanosheets array as a high-performance electrochemical water oxidation catalyst in alkaline solution, *Chem. Commun.* 53 (2017) 12446–12449.
- [10] X. Long, Z. Wang, S. Xiao, Y. An, S. Yang, Transition metal based layered double hydroxides tailored for energy conversion and storage, *Mater. Today* 19 (2016) 213–226.
- [11] Y.J. Yuan, Z.J. Ye, H.W. Lu, B. Hu, Y.H. Li, D.Q. Chen, J.S. Zhong, Z.T. Yu, Z.G. Zou, Comparing quasiparticle H_2O level alignment on anatase and rutile TiO_2 , *ACS Catal.* 6 (2015) 532–541.
- [12] H. Wang, H. Dai, Strongly coupled inorganic–nano-carbon hybrid materials for energy storage, *Chem. Soc. Rev.* 42 (2013) 3088–3113.
- [13] N. Yang, C. Tang, K.Y. Wang, G. Du, A.M. Asiri, X.P. Sun, Iron-doped nickel disulfide nanoarray: A highly efficient and stable electrocatalyst for water splitting, *Nano Res.* 9 (2016) 3346–3354.
- [14] J. Luo, et al., Water photolysis at 12.3% efficiency via perovskite photovoltaics and Earth-abundant catalysts, *Science* 345 (2014) 1593–1596.
- [15] W. He, Y. Yang, L. Wang, J. Yang, X. Xiang, D. Yan, F. Li, Enhanced photoelectrochemical water oxidation on a $BiVO_4$ photoanode modified with multi-functional layered double hydroxide nanowalls, *ChemSusChem* 8 (2015) 1568–1576.
- [16] R. Zhang, M. Shao, S. Xu, F. Ning, L. Zhou, M. Wei, Photo-assisted synthesis of zinc iron layered double hydroxides/ TiO_2 nanowires toward highly-efficient photoelectrochemical water splitting, *Nano Energy* 33 (2017) 21–28.
- [17] X. Lu, C. Zhao, Electrodeposition of hierarchically structured three-dimensional nickel–iron electrodes for efficient oxygen evolution at high current densities, *Nat. Commun.* 6 (2015) 6616.
- [18] M. Shao, F. Ning, M. Wei, D.G. Evans, X. Duan, Hierarchical nanowire arrays based on ZnO core-layered double hydroxide shell for largely enhanced photoelectrochemical water splitting, *Adv. Funct. Mater.* 24 (5) (2014) 580–586.
- [19] L. Wang, T. Sasaki, Titanium oxide nanosheets: graphene analogues with versatile functionalities, *Chem. Rev.* 114 (2014) 9455.
- [20] L. Zhou, Y. He, C. Jia, V. Pavlinek, P. Saha, Q. Cheng, Construction of hierarchical $CuO/Cu_2O@NiCo_2S_4$ nanowire arrays on copper foam for high performance supercapacitor electrodes, *Nanomaterials* (Basel) 7 (9) (2017) 273.
- [21] M. Shao, F. Ning, M. Wei, D.G. Evans, X. Duan, Hierarchical nanowire arrays based on ZnO core layered double hydroxide shell for largely enhanced photoelectrochemical water splitting, *Adv. Funct. Mater.* 24 (2014) 580–586.
- [22] H. Chen, Y. Gao, L. Sun, Highly active three-dimensional $NiFe/Cu_2O$ nanowires/Cu foam electrode for water oxidation, *ChemSusChem* 10 (2017) 1475–1481.
- [23] K. Zhang, W. Kim, M. Ma, X. Shi, J.H. Park, Tuning the charge transfer route by p–n junction catalysts embedded with CdS nanorods for simultaneous efficient hydrogen and oxygen evolution, *J. Mater. Chem. A* 3 (2015) 4803–4810.
- [24] J. Jin, J. Yu, G. Liu, P.K. Wong, Single crystal CdS nanowires with high visible-light photocatalytic H_2 -production performance, *J. Mater. Chem. A* 1 (2013) 10927–10934.
- [25] L. Cheng, Q. Xiang, Y. Liao, H. Zhang, CdS-based photocatalysts, *Energy Environ. Sci.* 11 (2018) 1362–1391.
- [26] Y. Li, L. Zhang, X. Xiang, D. Yan, F. Li, Engineering ZnCo-layered double hydroxide nanowalls toward high-efficiency electrochemical water oxidation, *J. Mater. Chem. A* 2 (2014) 13250–13258.
- [27] N.K. Chaudhari, H. Jin, B. Kim, K. Lee, Nanostructured materials on 3D nickel foam as electrocatalysts for water splitting, *Nanoscale* 9 (2017) 12231–12247.
- [28] J. Yu, J. Liu, A. Clearfield, J.E. Sims, M.T. Speigle, S.L. Suib, L. Sun, Synthesis of layered double hydroxide single-layer nanosheets in formamide, *Inorg. Chem.* 55 (22) (2016) 12036–12041.
- [29] S.H. Ahn, I. Choi, H.-Y. Park, S.J. Hwang, S.J. Yoo, E. Cho, H.-J. Kim, D. Henkensmeier, S.W. Nam, S.-K. Kim, J.H. Jang, Effect of morphology of electrodeposited Ni catalysts on the behavior of bubbles generated during the oxygen evolution reaction in alkaline water electrolysis, *J. Chem. Commun.* 49 (2013) 9323–9325.
- [30] M. Shao, Z. Li, R. Zhang, F. Ning, M. Wei, D.G. Evans, X. Duan, Hierarchical conducting polymer@clay core-shell arrays for flexible all-solid-state supercapacitor devices, *Small* 11 (2015) 3530–3538.
- [31] D.H. Wang, L. Wang, A.W. Xu, Room-temperature synthesis of $Zn_{0.80}Co_{0.20}S$ solid solution with a high visible-light photocatalytic activity for hydrogen evolution, *Nanoscale* 4 (2012) 2046–2053.
- [32] J.F. Moulder, W.F. Stickle, P.E. Sobol, K.D. Bomben, Handbook of X-ray photoelectron spectroscopy reference book of standard spectra for identification and interpretation of XPS data, *Phys. Electron.* (1995) 230–232.
- [33] G. Yang, B. Yang, T. Xiao, Z. Yan, One-step solvothermal synthesis of hierarchically porous nanostructured CdS/TiO_2 heterojunction with higher visible light photocatalytic activity, *Appl. Surf. Sci.* 283 (2013) 402–410.
- [34] B. Weng, F. Xu, C. Wang, W. Meng, C.R. Grice, Y. Yan, Layered $Na_{1-x}Ni_yFe_{1-y}O_2$ double oxide oxygen evolution reaction electrocatalyst for highly efficient water splitting, *Energy Environ. Sci.* 10 (2017) 121–128.
- [35] N. Jiang, B. You, M. Sheng, Y. Sun, Electrodeposited cobalt-phosphorous-derived films as competent bifunctional catalysts for overall water splitting, *Angew. Chem. Int. Ed.* 54 (2015) 6251–6254.
- [36] F. Song, X. Hu, Ultrathin cobalt–Manganese layered double hydroxide is an efficient oxygen evolution catalyst, *J. Am. Chem. Soc.* 136 (2014) 16481–16484.
- [37] J. Bao, X. Zhang, B. Fan, J. Zhang, M. Zhou, W. Yang, X. Hu, H. Wang, B. Pan, Y. Xie, Ultrathin spinel-structured nanosheets rich in oxygen deficiencies for enhanced electrocatalytic water oxidation, *Angew. Chem. Int. Ed.* 54 (2015) 7399–7404.
- [38] C.C.L. McCrory, S. Jung, I.M. Ferrer, S.M. Chatman, J.C. Peters, T.F. Jaramillo, Benchmarking hydrogen evolving reaction and oxygen evolving reaction electrocatalysts for solar water splitting devices, *J. Am. Chem. Soc.* 137 (13) (2015) 4347–4357.
- [39] Y. Liang, Y. Li, H. Wang, J. Zhou, J. Wang, T. Regier, H. Dai, Co_3O_4 nanocrystals on graphene as a synergistic catalyst for oxygen reduction reaction, *Nat. Mater.* 10 (2011) 780–786.
- [40] F. Song, X. Hu, Exfoliation of layered double hydroxides for enhanced oxygen evolution catalysis, *Nat. Commun.* 5 (2014) 4477–4477.
- [41] B.M. Hunter, J.D. Blakemore, M. Deimund, H.B. Gray, J.R. Winkler, A.M. Müller,

- Highly active mixed-metal nanosheet water oxidation catalysts made by pulsed-laser ablation in liquids, *J. Am. Chem. Soc.* 136 (2014) 13118–13121.
- [42] H. Jin, J. Wang, D. Su, Z. Wei, Z. Pang, Y. Wang, In situ cobalt-cobalt oxide/N-doped carbon hybrids as superior bifunctional electrocatalysts for hydrogen and oxygen evolution, *J. Am. Chem. Soc.* 137 (2015) 2688–2694.
- [43] T. Ma, S. Dai, M. Jaroniec, S.Z.J. Qiao, Metal-organic framework derived hybrid Co_3O_4 -carbon porous nanowire arrays as reversible oxygen evolution electrodes, *J. Am. Chem. Soc.* 136 (2014) 13925–13931.
- [44] Y. Tang, X. Fang, X. Zhang, G. Fernandes, Y. Yan, D. Yan, X. Xiang, J. He, A space-confined earth-abundant bifunctional electrocatalyst for high-efficiency water splitting, *ACS Appl. Mater. Interfaces* 9 (42) (2017) 36762–36771.
- [45] L. Xie, X. Ren, Q. Liu, G. Cui, R. Ge, A.M. Asiri, X. Sun, Q. Zhang, L. Chen, $\text{Ni}(\text{OH})_2$ - PtO_2 hybrid nanosheet array with ultralow Pt loading toward efficient and durable alkaline hydrogen evolution, *J. Mater. Chem. A* 6 (2018) 1967–1970.
- [46] N. Chouhan, R.S. Liu, J. Zhang, New York, Water Splitting Materials and Applications, CRC Press Taylor & Francis Group, 2017, pp. 33487–33742.
- [47] B. Zhang, C. Xiao, S. Xie, J. Liang, X. Chen, Y. Tang, Iron-nickel nitride nanostructures in situ grown on surface-redox-etching nickel foam: efficient and ultra-sustainable electrocatalysts for overall water splitting, *Chem. Mater.* 28 (2016) 6934–6941.
- [48] K. Liu, H. Zhong, F. Meng, X. Zhang, J. Yan, Q. Jiang, Recent advances in metal nitrogen-carbon catalysts for electrochemical water splitting, *Mater. Chem. Front.* 1 (2017) 2155–2173.
- [49] R. Xu, R. Wu, Y. Shi, J. Zhang, B. Zhang, Ni_3Se_2 nanoforest/Ni foam as a hydrophilic, metallic, and self-supported bifunctional electrocatalyst for both H_2 and O_2 generations, *Nano Energy* 24 (2016) 103–110.
- [50] J. Xing, H. Li, M.M.C. Cheng, S.M. Geyer, K.Y.S. Ng, Electro-synthesis of 3D porous hierarchical Ni-Fe phosphate film/Ni foam as a high-efficiency bifunctional electrocatalyst for overall water splitting, *J. Mater. Chem. A* 4 (2016) 13866–13873.
- [51] X.D. Wang, H.Y. Chen, Y.F. Xu, J.F. Liao, B.X. Chen, H.S. Rao, D.B. Kuang, C.Y. Su, Self-supported NiMoP_2 nanowires on carbon cloth as an efficient and durable electrocatalyst for overall water splitting, *J. Mater. Chem. A* 5 (2017) 7191–7199.
- [52] J. Li, G. Wei, Y. Zhu, Y. Xi, X. Pan, Y. Ji, I.V. Zatovsky, W. Han, Hierarchical NiCoP nanocone arrays supported on Ni foam as an efficient and stable bifunctional electrocatalyst for overall water splitting, *J. Mater. Chem. A* 5 (2017) 14828–14837.
- [53] Y. Tan, H. Wang, P. Liu, Y. Shen, C. Cheng, A. Hirata, T. Fujita, Z. Tang, M. Chen, Versatile nanoporous bimetallic phosphides towards electrochemical water splitting, *Energy Environ. Sci.* 9 (2016) 2257–2261.
- [54] X. Ji, R. Zhang, X. Shi, A.M. Asiri, B. Zheng, X. Sun, Fabrication of hierarchical CoP nanosheet@microwire array via space-confined phosphidation toward high-efficiency water oxidation electrocatalysis under alkaline conditions, *Nanoscale* 10 (2018) 7941–7945.
- [55] M. Xie, X. Xiong, L. Yang, X. Shi, A.M. Asiri, X. Sun, $\text{Fe}(\text{TCNQ})_2$ nanowires array on Fe foil: an efficient non-noble metal catalyst for the oxygen evolution reaction in alkaline media, *Chem. Commun.* 54 (2018) 2300–2303.
- [56] Z.Y. Yu, Y. Duan, M.R. Gao, C.C. Lang, Y.R. Zheng, S.H. Yu, A one dimensional porous carbon-supported $\text{Ni}/\text{Mo}_2\text{C}$ dual catalyst for efficient water splitting, *Chem. Sci.* 8 (2017) 968–973.
- [57] K. Qu, Y. Zheng, Y. Jiao, X. Zhang, S. Dai, S.Z. Qiao, Polydopamine-inspired, dual heteroatom-doped carbon nanotubes for highly efficient overall water splitting, *Adv. Energy Mater.* 7 (2017) 1602068–1602075.
- [58] X. Xiong, C. You, Z. Liu, A.M. Asiri, X. Sun, Co-doped CuO nanoarray: an efficient oxygen evolution reaction electrocatalyst with enhanced activity, *ACS Sustainable Chem. Eng.* 6 (3) (2018) 2883–2887.
- [59] L. Yu, H. Zhou, J. Sun, F. Qin, F. Yu, J. Bao, Y. Yu, S. Chen, Z. Ren, Cu nanowires shelled with NiFe layered double hydroxide nanosheets as bifunctional electrocatalysts for overall water splitting, *Energy Environ. Sci.* 10 (2017) 1820–1827.
- [60] F. Yu, H. Zhou, Z. Zhu, Jg. Sun, R. He, J. Bao, S. Chen, Z. Ren, Three-dimensional nanoporous iron nitride film as an efficient electrocatalyst for water oxidation, *ACS Catal.* 7 (2017) 2052–2057.
- [61] H. Liang, A.N. Gandi, C. Xia, M.N. Hedhili, D.H. Anjum, U. Schwingenschlög, H.N. Alshareef, Amorphous $\text{NiFe-OH}/\text{NiFeP}$ electrocatalyst fabricated at low temperature for water oxidation applications, *ACS Energy Lett.* 2 (5) (2017) 1035–1042.
- [62] C. Shu, S. Kang, Y. Jin, X. Yue, P.K. Shen, Bifunctional porous non-precious metal WO_2 hexahedral networks as an electrocatalyst for full water splitting, *J. Mater. Chem. A* 5 (2017) 9655–9660.
- [63] Y. Tang, R. Wang, Y. Yang, D. Yan, X. Xiang, Highly Enhanced Photoelectrochemical Water Oxidation Efficiency Based on Triadic Quantum Dot/Layered Double Hydroxide/ BiVO_4 Photoanodes, *ACS Appl. Mater. Interfaces* 8 (30) (2016) 19446–19455.
- [64] L. Yao, D. Wei, D. Yan, C. Hu, ZnCr layered double hydroxide (LDH) nanosheets assisted formation of hierarchical flower-like CdZnS@LDH microstructures with improved visible-light-driven H_2 production, *Chem. Asian J.* 10 (3) (2015) 630–636.
- [65] W. Zhen, X. Ning, B. Yang, Y. Wu, Z. Li, G. Lu, The enhancement of CdS photocatalytic activity for water splitting via anti-photocorrosion by coating Ni_2P shell and removing nascent formed oxygen with artificial gill, *Appl. Catal. B-Environ.* 221 (2018) 243–257.
- [66] T. Kameyama, K. Okazaki, K. Takagi, T. Torimoto, Stacked-structure-dependent photoelectrochemical properties of CdS nanoparticle/layered double hydroxide (LDH) nanosheet multilayer films prepared by layer-by-layer accumulation, *Phys. Chem. Chem. Phys.* 11 (2009) 5369–5376.
- [67] C. Jiang, S.J.A. Moniz, A. Wang, T. Zhang, J. Tang, Photoelectrochemical devices for solar water splitting – materials and challenges, *Chem. Soc. Rev.* 46 (2017) 4645–4660.